SUPPLEMENTARY MATERIALS

Tunable phononic coupling in excitonic quantum emitters

Adina Ripin[1], Ruoming Peng[2*], Xiaowei Zhang[3], Srivatsa Chakravarthi[1], Minhao He[1], Xiaodong Xu[1,3], Kai-Mei Fu[1,2], Ting Cao[3], and Mo Li[1,2,*]

[1]*Department of Physics, University of Washington, Seattle, WA 98195, USA*

[2]*Department of Electrical and Computer Engineering, University of Washington, Seattle, WA 98195, USA*

[3]*Department of Material Science and Engineering, University of Washington, Seattle, WA 98195, USA*

** pruoming@uw.edu*

**moli96@uw.edu*

Supplementary Table 1. Summary of IX quantum emitters

Emitter	Device	Type	Energy tuning range (meV)	Min Energy (meV)	Max Energy (meV)	Resolved Phonon Lines
QE1	A	interlayer	6.35	1547.0	1553.4	yes
QE3	A	interlayer	11.5	1520.0	1531.5	yes
QE4	A	interlayer	6.26	1549.9	1556.2	yes
QE5	A	interlayer	9.75	1490.6	1500.4	yes
QE6	A	interlayer	6.96	1522.2	1529.2	yes
QE7	B	interlayer	11.6	1543.8	1555.4	yes
QE8	B	interlayer	12.8	1494.2	1507.0	no
QE9	C	interlayer	8.61	1494.1	1502.7	no
QE10	D	interlayer	8.43	1502.8	1511.3	no

Supplementary Figure 1. Photoluminescence (PL) spectra of nine IX QEs in our samples.

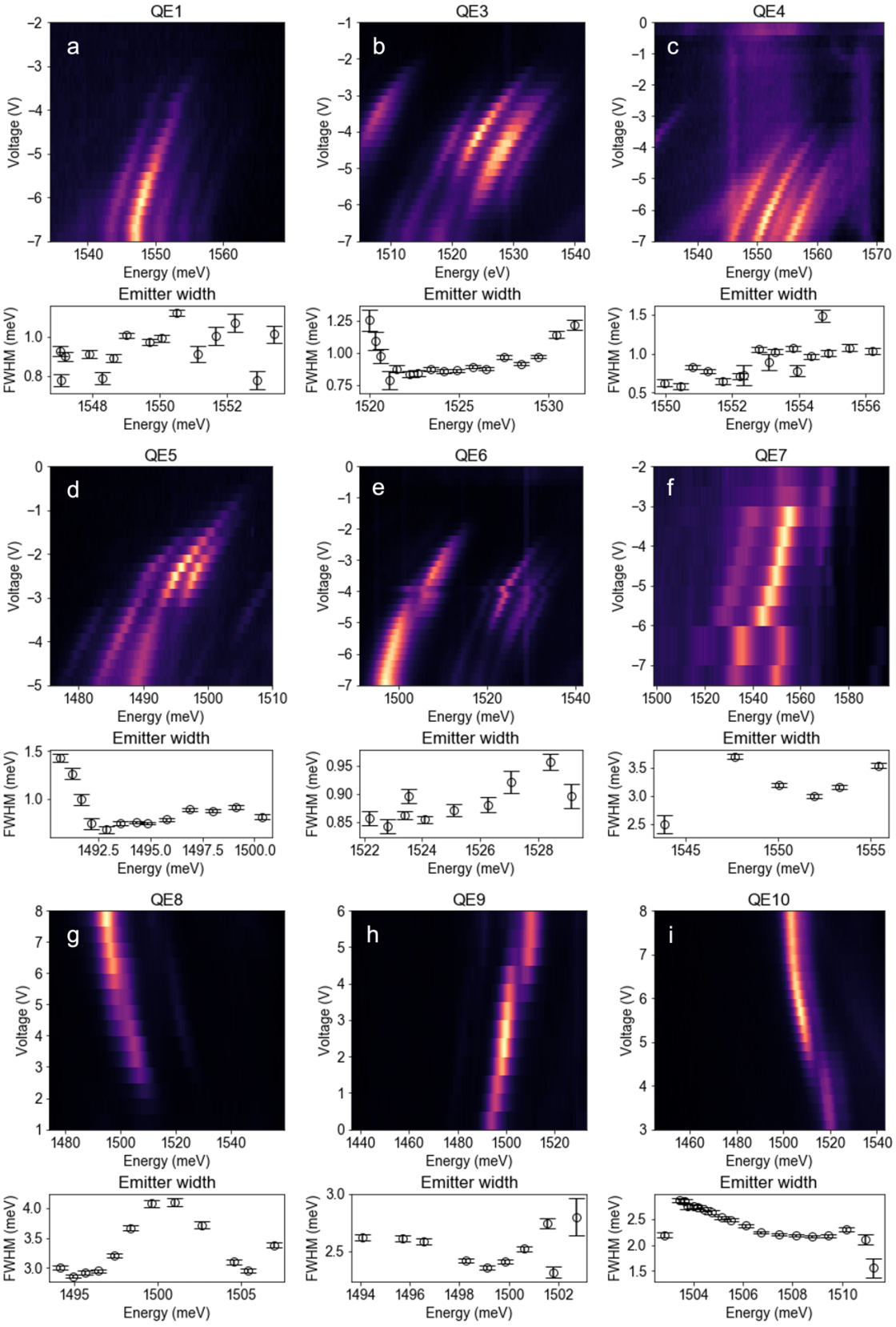

Supplementary Table 2. Summary of intralayer exciton QEs

Emitter	Device	Type	Linewidth Change (meV)	Min Linewidth (meV)	Max Linewidth (meV)	Resolved Phonon Lines
QE2	C	intralayer	0.53	0.94	1.45	yes
QE11	D	intralayer	0.73	1.62	2.37	yes
QE12	D	intralayer	0.39	1.95	2.34	no

Supplementary Figure 2. PL spectra of three intralayer exciton QEs in our samples.

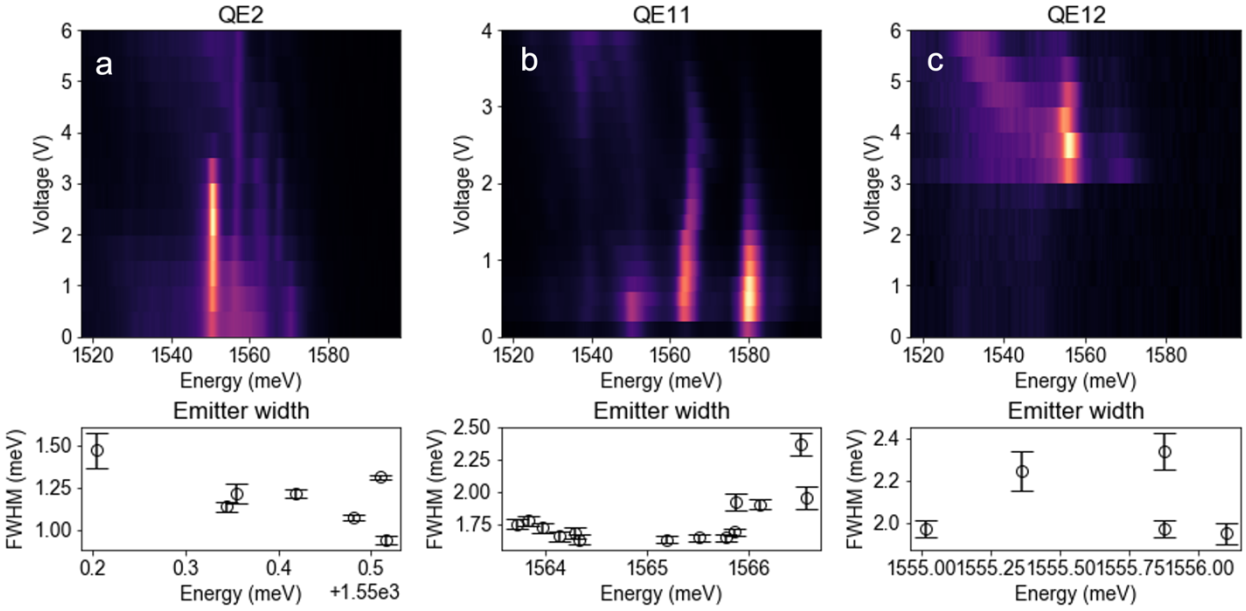

Supplementary Note 1. Second-order correlation $g^{(2)}$ measurements of 2D emitters

To confirm that the QEs emit single photons, we performed measurements of the second-order correlation function $g^{(2)}$ using a pair of single-photon Si avalanche photodetectors (SPAPDs) and a Time-Correlated Single-Photon Counting (TCSPC) module. A tunable bandpass filter was used to select the signal within the frequency range highlighted in red in Supplementary Figures 3a and c. The filtered signal was then split with a beam splitter to the two SPAPDs, which were connected to the TCSPC. The $g^{(2)}$ was plotted as a function of the time lag between triggering events of the two SPADs[1–3].

The results in Supplementary Figures 3b and d clearly show the characteristic dip of $g^{(2)}$ at zero delay, with $g^2(0)<0.5$ signaling the non-classical anti-bunching behavior. The data in black was fit with the function $g^2(\tau) = 1 - \alpha \cdot e^{-\tau/T}$, where τ is the time delay between photon detections, and T is the lifetime of the exciton. $\alpha = SBR^2/(1 + \mathrm{SBR})^2$ is the normalization factor, where SBR is the signal-to-background ratio[1,4]. With this fit, we can estimate the $g^{(2)}(0)$, as well as the exciton lifetime T, as reported in the main text.

From all the 2D QEs we have measured, we found that the linewidth of PL peaks is a good indicator to classify whether an emitter is a single-photon emitter. In Supplementary Figures 3a and c, we found these emitters have a linewidth of a few meV (1.65 meV for QE11, 2.34 meV for QE12), in comparison to the exciton linewidth in WSe_2, which is > 10meV[5,6]. Both emitters have $g^{(2)}(0)<0.5$, classifying them as single-photon emitters. Therefore, we considered a linewidth of 2.4 meV as the upper bound for single-photon emitters in our samples. We thus conclude that all of the emitters presented in the main text and Supplementary Figures 1 and 2 can be classified as single-photon emitters. Furthermore, in Supplementary Figures 3a and c, we note that the filter passband includes a nontrivial amount of background signal, yet still has a very low $g^{(2)}(0)$. This further supports our conclusion that the set of multiple emission lines is originating from phonon coupling to a single QE.

Supplementary Figure 3. Second-order correlation measurements of 2D emitters. (a, c) PL spectra (black) of two emitters (QE11 and QE12). The dashed lines are Lorentzian fitting. The passband of the tunable filter used in the g^2 measurements is indicated with the red shaded area. **(b, d)** Second-order correlation measurements of the two emitters. The low $g^2(0)$ values show their single-photon characteristics with high purity.

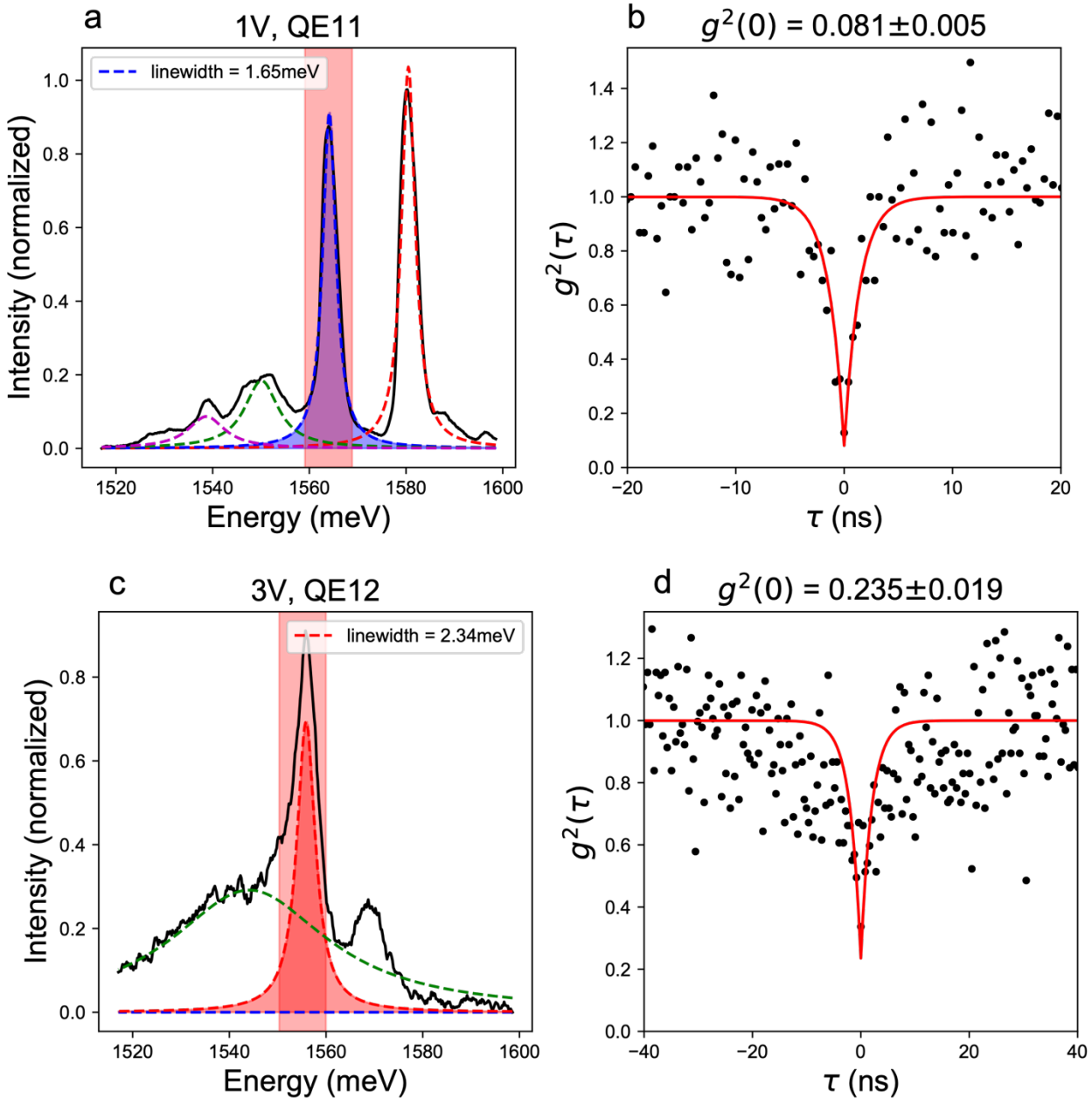

Supplementary Note 2. Polarization-resolved measurements for single phonon lines

The polarization measurements of the QEs (Figure 3c and d in the main text, Supplementary Figure 4) were conducted with a linear polarizer mounted on a rotation stage in the signal path. The results were processed by fitting Lorentzian functions to the PL peaks to extract the central energy and peak intensity of each emission line. The amplitude of each peak at different polarization angles θ was plotted to show the angular dependence. The curve of a perfectly linearly polarized emitter ($\cos^2(\theta)$) is also plotted as eye guidance.

The polarization data for two additional QEs (QE4 and QE6) are shown in Supplementary Figure 4, similar to Figures 3c and d in the main text, further supporting that each emission line has shown the same linear polarization. Because emitters from strained 2D materials have a randomly oriented linear polarization, these results strongly support our claims that these lines originate from the same emitter[1,4,7–9].

Supplementary Figure 4. Polarization of each phonon line for two additional single phonon lines. Similar to the phonon lines shown in the main text, all the emission lines have the same linear polarization, confirming these peaks originate from the same source.

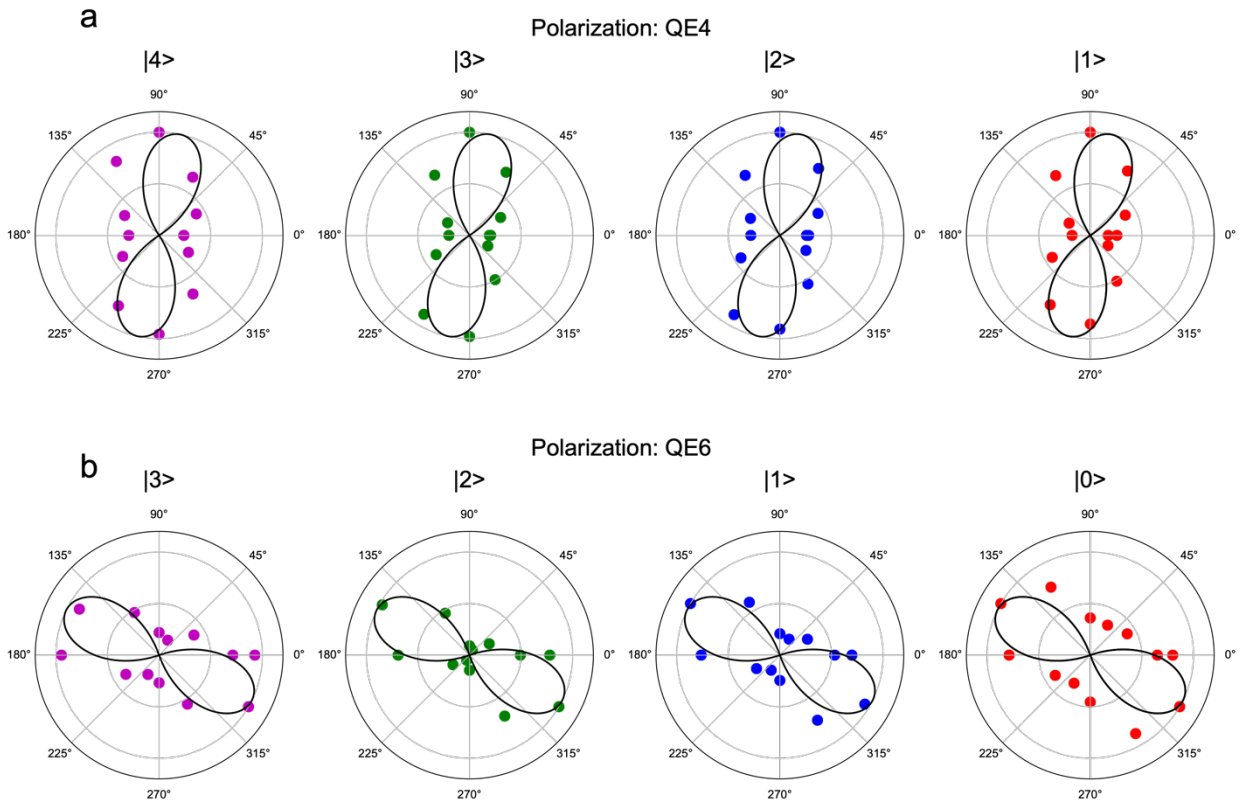

Supplementary Note 3. Power dependence of different phonon lines in QEs

We further characterized the power-dependent PL of the QEs by changing the pump laser power at a fixed gate voltage. The PL was then fit with Lorentzian functions to find the central energy for each phonon line. The peak amplitude at that energy was then extracted for different pump powers. From the results, we observe a trend that the higher-order phonon lines (lower energy states) saturate at a lower pump power than the lower-order phonon lines (higher energy states). This trend is consistent for all emission lines in QE3, as shown in Supplementary Figure 5. The saturation behaviors can be attributed to the lifetime limited excited state considering the nature of the localized quantum emitters[10,11].

Supplementary Figure 5. Power dependence of the 5 phonon lines from QE3. The measured data is shown as black symbols. The data is fit with linear functions (dashed lines) in two regions. The colors of the lines correspond to the phonon lines in Supplementary Figure 6b.

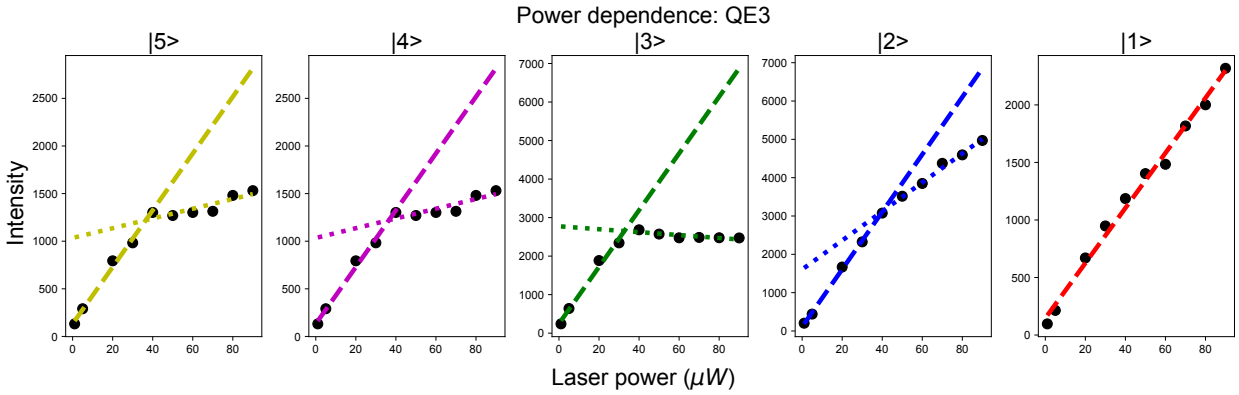

Supplementary Note 4. The single phonon lines in IX QEs coupled to breathing mode phonons

The Huang-Rhys parameter *S* is determined by fitting the series of phonon peaks with Lorentz functions and extracting the amplitude of each peak. Those peak amplitudes follow the Poisson function according to the Huang-Rhys theory:

$$f(n, S) = e^{-S} S^n / n!$$

where n is the number of phonons[12]. The highest observable energy peak was assigned with the lowest phonon number n_0, the second-highest energy peak was assigned n_0+1, and so on. The peak intensities were then fit with the Poisson function above with n_0 and S as free parameters with an upper limit of n_0=3. Once n_0 was determined for a given QE, it was fixed and the peak amplitudes were fit with a Poisson distribution to determine *S.*

In Supplementary Figure 6, the fitting results are shown with the black stars. To be identified as one of these phonon states, the peaks must behave the same with voltage modulation (i.e. tuning at the same rate, appearing at the same voltage), and have the same linear polarization. As listed in Supplementary Table 3, the calculated *S* ranges between 1.0-6.0. The Poisson fitting is not ideal with a large error. The phonon lines are not evenly spaced and the amplitudes deviate from the ideal Poisson distribution. This discrepancy is caused by the approximate treatment of exciton-phonon coupling in the Huang-Rhys theory, including approximating the exciton states as harmonic oscillators and assuming linear coupling between the exciton and phonon states. The interplay of the excitonic band structures of WSe_2 and local strain due to the nanopillar and breathing phonon modes can increase the complexity of the problem further. Nevertheless, the analysis qualitatively determines the *S* value, showing a clear trend when it is tuned by the gate voltage (Fig. 4c in the main text).

Emitters in Supplementary Figure 6 have phonon line spacing in the range of 3.0 to 5.0 meV. This variation of phonon energy can be attributed to several reasons. First, as discussed in the main text, there are three interlayer breathing modes for TMDs encapsulated with hBN due to the interface phonon mode hybridization[13,14]. Second, as shown by the phonon band calculations (Supplementary Figure 7), the strain induced by the nanopillar will modulate interlayer separation of the bilayer WSe_2, resulting in a shift of the breathing mode energy, as shown in Supplementary Figure 8. The calculation results support that these energy spacings are well within the expected range.

Supplementary Table 3. The calculated Huang-Rhys Parameter and the phonon line spacings of IX QEs.

Emitter	Huang-Rhys Parameter	Phonon line spacing in energy
QE1	$S = 6.15 \pm 0.47$	$n = 1 \rightarrow 2$: 3.00meV $n = 2 \rightarrow 3$: 3.32meV $n = 3 \rightarrow 4$: 3.71meV $n = 4 \rightarrow 5$: 3.70meV
QE3	$S = 1.32 \pm 0.39$	$n = 0 \rightarrow 1$: 4.19meV $n = 1 \rightarrow 2$: 5.10meV $n = 2 \rightarrow 3$: 3.70meV $n = 3 \rightarrow 4$: 3.76meV
QE4	$S = 1.64 \pm 0.54$	$n = 1 \rightarrow 2$: 3.10meV $n = 2 \rightarrow 3$: 2.63meV $n = 3 \rightarrow 4$: 4.43meV
QE6	$S = 2.64 \pm 0.15$	$n = 0 \rightarrow 1$: 4.14meV $n = 1 \rightarrow 2$: 5.15meV $n = 2 \rightarrow 3$: 4.07meV

Supplementary Figure 6. **The phonon lines in IX QEs coupled to breathing mode phonons.** Each peak is fit with a Lorentzian function shown as shaded areas. The amplitude of each peak was fit with a Poisson function to extract the Huang-Rhys parameter, shown as black stars.

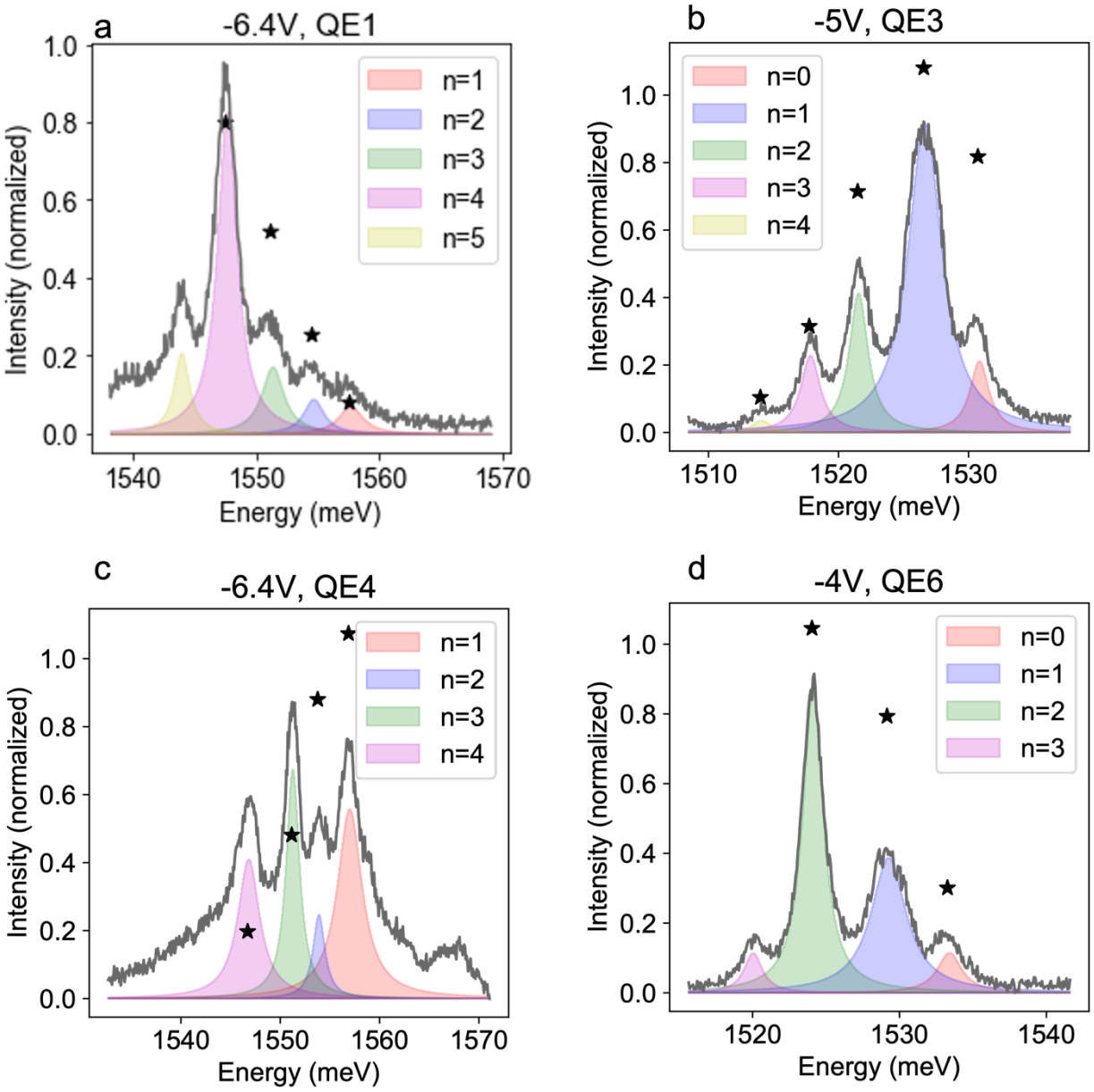

Supplementary Note 5. Strain modulation of interlayer breathing mode phonon

The local strain induced by nanopillars not only creates local potential wells to trap IXs, but also strongly modulates the interlayer phonon modes, causing an energy shift of the breathing mode (BM) phonon. It is computationally impractical to directly simulate the strain caused by nanopillars and then calculate the phonon energies. To simplify the problem, we choose different interlayer distances and lattice constants for the unit cell of bilayer WSe_2. and then calculate the phonon energies of the BM using the first-principles density-functional perturbation theory. Supplementary Figure 8a shows the BM phonon energy variations under different in-plane strains. Supplementary Figure 8b shows the BM phonon energies at different interlayer distances around the equilibrium interlayer distance. It can be seen that the BM phonon energy weakly depends on the in-plane strain but strongly depends on the inter-layer distance. It indicates that the out-of-plane strain due to nanopillars can significantly modulate BM phonon energy. The calculated energy variation range of the BM phonon is consistent with the energy spacing range as in Supplementary Table 3 and Supplementary Figure 6. The BM phonon couples strongly with the IXs by directly modulating the interlayer distance.

Supplementary Figure 7. Phonon dispersion of intrinsic bilayer WSe_2.

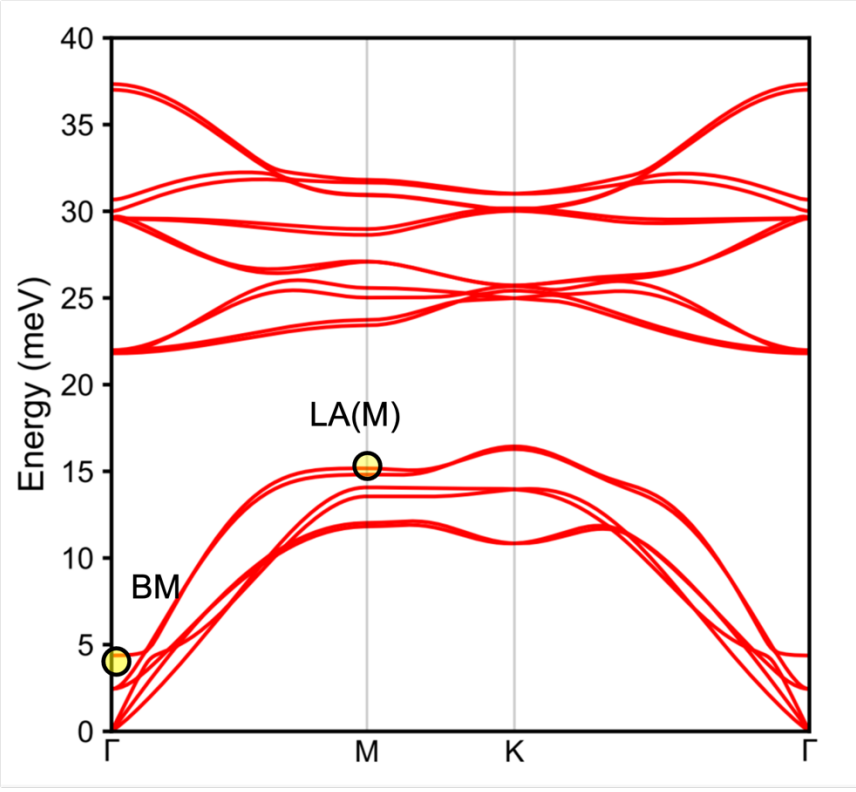

Supplementary Figure 8. Modulation of interlayer BM phonon energy. (a) BM phonon energy dependence on the in-plane strain. (b) BM phonon energy dependence on the W-W interlayer distance. The equilibrium interlayer distance is 6.417 Å.

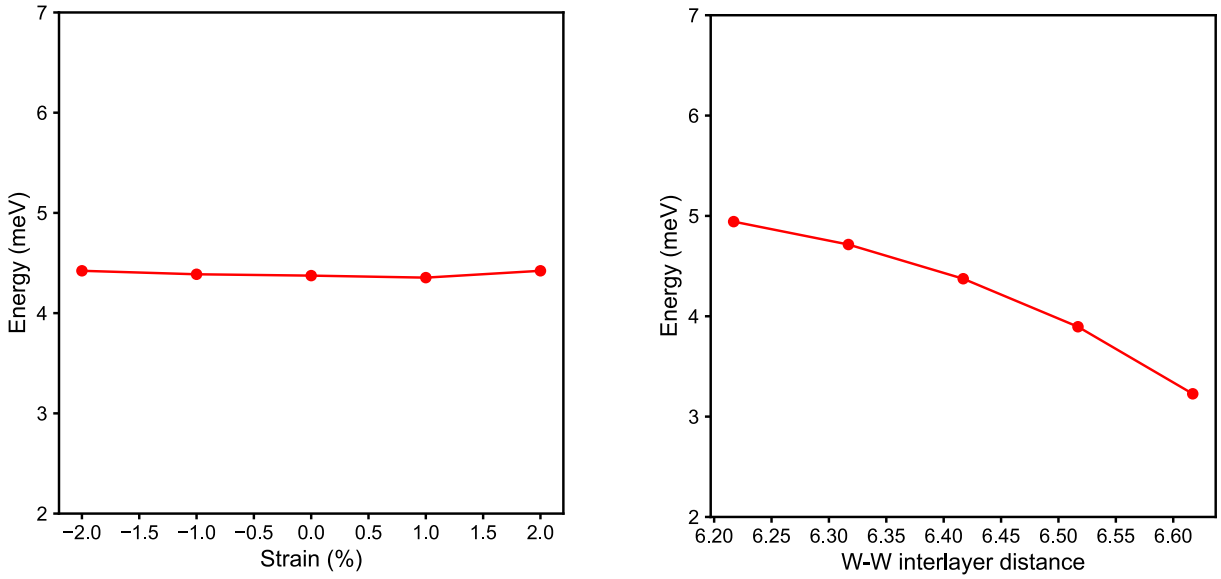

Supplementary Note 6. The IX QEs coupling to other phonon modes

Supplementary Figure 9 shows PL spectra from QE7, which have phonon lines with energy spacing in the range of 10.0-16.0 meV, much larger than the BM phonon energy. We attribute these phonon lines to other lattice phonon modes such as the LA(M) phonon, which has an energy of 15.3 meV in pristine bilayer WSe_2[13]. Typically, LA(M) phonons are only observed in Raman measurements of monolayer WSe_2 because they require inelastic scattering processes at structural defects or along the edges of the flake. However, our emitters are created by a combination of localized strain and defects under a large tensile strain. The modified band structure increases the strength of the LA(M) phonon, and in certain cases, allows it to couple to IXs. Nevertheless, the LA(M) phonon lines are much less frequently observed than the BM phonon lines.

Because of the much higher energy of the LA(M) than the BM phonons, it would follow that the anharmonic effects are more apparent when excitons are coupled to them, which could explain the large variation of phonon line spacings as listed in Supplementary Table 4. Another possible explanation is that the IXs couple to hybridization of different phonon modes with varying energy.

Supplementary Table 4: The phonon lines in IX QEs coupled to the higher-energy phonon mode

Emitter	Huang-Rhys Parameter	Phonon line spacing in energy
QE7	$S = 5.92 \pm 0.34$	$n = 1 \rightarrow 2$: 15.58meV $n = 2 \rightarrow 3$: 14.73meV $n = 3 \rightarrow 4$: 10.77meV $n = 4 \rightarrow 5$: 16.14meV

Supplementary Figure 9. **The phonon lines observed in IX QEs with larger energy spacing.** Each peak is fit with a Lorentzian function shown as shaded areas. The amplitude of each peak was fit with a Poisson function to extract the Huang-Rhys parameter, shown as black stars.

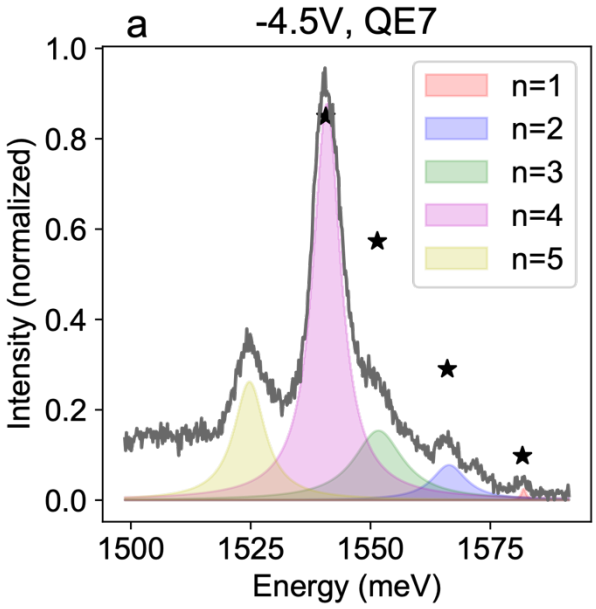

Supplementary Note 7. The phonon lines of intralayer exciton in QEs

In rare cases, we also observed phonon lines in QEs with only intralayer exciton emission, which is shown in Supplementary Figure 10. The coupling between the lattice phonon and the intralayer exciton is not expected to happen in pristine bilayer WSe_2. But the local strain effect, materials defects, and the local charging effect may enable the coupling between intralayer exciton and lattice phonon modes (shear mode and LA(M)).

Supplementary Table 5. The energy spacing between phonon lines of intralayer exciton in QEs

Emitter	Huang-Rhys Parameter	Peak-to-peak energy spacing
QE2	$S = 5.24 \pm 0.60$	$n = 1 \rightarrow 2$: 5.53meV $n = 2 \rightarrow 3$: 5.15meV $n = 3 \rightarrow 4$: 6.61meV
QE11	$S = 1.59 \pm 0.26$	$n = 1 \rightarrow 2$: 16.36meV $n = 2 \rightarrow 3$: 13.31meV $n = 3 \rightarrow 4$: 11.87meV $n = 4 \rightarrow 5$: 7.53meV

Supplementary Figure 10. The phonon lines of intralayer exciton in QEs. Each peak is fit with a Lorentz function shown in dashed colored lines, and the intensity of each peak was fit with a Poisson function to extract the Huang-Rhys parameter, shown in black stars.

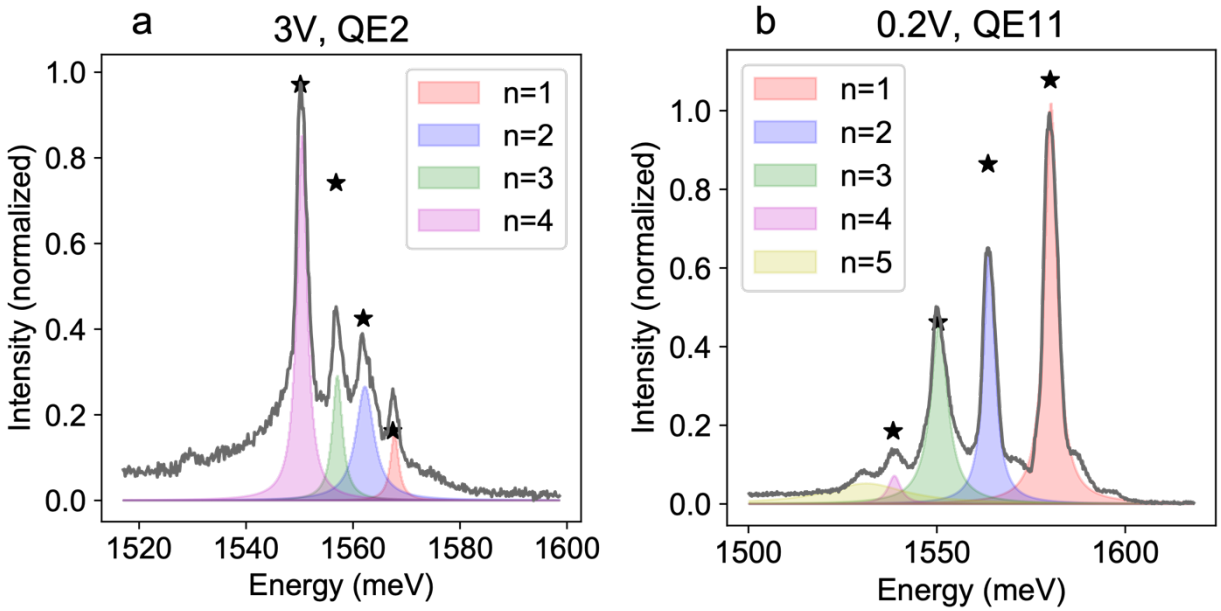

REFERENCES

1. Branny, A., Kumar, S., Proux, R. & Gerardot, B. D. Deterministic strain-induced arrays of quantum emitters in a two-dimensional semiconductor. *Nature Communications* **8**, 15053 (2017).

2. Peyskens, F., Chakraborty, C., Muneeb, M., van Thourhout, D. & Englund, D. Integration of single photon emitters in 2D layered materials with a silicon nitride photonic chip. *Nature Communications* **10**, 4435 (2019).

3. Baek, H. *et al.* Highly energy-tunable quantum light from moiré-trapped excitons. *Science Advances* **6**, (2020).

4. Linhart, L. *et al.* Localized Intervalley Defect Excitons as Single-Photon Emitters in WSe2. *Physical Review Letters* **123**, 146401 (2019).

5. Aslan, O. B., Deng, M., Brongersma, M. L. & Heinz, T. F. Strained bilayer WSe2 with reduced exciton-phonon coupling. *Physical Review B* **101**, 115305 (2020).

6. Lindlau, J. *et al.* The role of momentum-dark excitons in the elementary optical response of bilayer WSe2. *Nature Communications* **9**, 2586 (2018).

7. Koperski, M. *et al.* Single photon emitters in exfoliated WSe2 structures. *Nature Nanotechnology* **10**, 503–506 (2015).

8. Li, W., Lu, X., Dubey, S., Devenica, L. & Srivastava, A. Dipolar interactions between localized interlayer excitons in van der Waals heterostructures. *Nature Materials* **19**, 624–629 (2020).

9. Lu, X. *et al.* Optical initialization of a single spin-valley in charged WSe2 quantum dots. *Nature Nanotechnology* **14**, 426–431 (2019).

10. Allen, L. & Eberly, J. *Optical Resonance and Two-Level Atoms*. (Dover, 1988).

11. Tonndorf, P. *et al.* Single-photon emission from localized excitons in an atomically thin semiconductor. *Optica* **2**, 347 (2015).

12. Kelley, A. M. Exciton-optical phonon coupling in II-VI semiconductor nanocrystals. *The Journal of Chemical Physics* **151**, 140901 (2019).

13. Jeong, T. Y. *et al.* Coherent Lattice Vibrations in Mono- and Few-Layer WSe2. *ACS Nano* **10**, 5560–5566 (2016).

14. Grzeszczyk, M. *et al.* Breathing modes in few-layer MoTe $_2$ activated by h-BN encapsulation. *Applied Physics Letters* **116**, 191601 (2020).